


 Cite this: *RSC Adv.*, 2022, 12, 27839

# Zinc ion detection using a benzothiazole-based highly selective fluorescence “turn-on” chemosensor and its real-time application†

 Saravanan Enbanathan,<sup>a</sup> Sathishkumar Munusamy,<sup>b</sup> Dhanapal Jothi,<sup>a</sup> Selin Manojkumar,<sup>a</sup> Saravanakumar Manickam<sup>c</sup> and Sathiyarayanan Kulathu Iyer<sup>\*,a</sup>

A new photochromic fluorescence chemosensor was devised and effectively synthesized using benzothiazole and imidazopyridine derivatives. A “turn-on” fluorescence sensor BIPP for Zn<sup>2+</sup> detection was developed and has a quick response, excellent sensitivity, and remarkable selectivity over other metal ions. When Zn<sup>2+</sup> was added to the BIPP solution, a new strong fluorescence emission peak at 542 nm formed with a considerable increase in intensity. The fluorescence color of the BIPP solution changed from blue to bright green. The binding ratio 8 : 2 was found between BIPP and Zn<sup>2+</sup> by the results of Job's plot, HRMS and <sup>1</sup>H-NMR. The detection limit (LOD) of BIPP towards Zn<sup>2+</sup> was determined to be 2.36 × 10<sup>-8</sup>, which is remarkably low. The ability to detect Zn<sup>2+</sup> in real water samples demonstrates that BIPP may also be used in environmental systems. Additionally, BIPP can be used to measure Zn<sup>2+</sup> levels in living cells.

 Received 5th August 2022  
 Accepted 19th September 2022

DOI: 10.1039/d2ra04874d

[rsc.li/rsc-advances](http://rsc.li/rsc-advances)

## 1. Introduction

The development of chemosensors capable of detecting a wide variety of metal ions and anions has generated considerable attention due to their wide range of biological, therapeutic, and industrial applications.<sup>1–6</sup> Among them, the zinc (Zn<sup>2+</sup>) ion is the second most common transition metal element in humans after iron, making it a critical mineral in biological processes. The benefits of zinc include support for the immune system, regulation of hormones and digestion, and many proteins and enzymes that consist of Zn<sup>2+</sup>-ions as a cofactor have been discovered.<sup>7–9</sup> The elevated levels of zinc ions, on the other hand, have been related to a variety of neurological diseases, including arteriosclerosis,<sup>7</sup> Parkinson's disease,<sup>10,11</sup> and epilepsy.<sup>12,13</sup> On the contrary, zinc shortage in the body may cause health issues including growth retardation, diarrhoea, poor wound healing, and dermatitis. The Zn<sup>2+</sup> ion concentration in human excretion varies widely depending on a variety of factors, including biological, habitual, and environmental factors. Therefore, zinc content assessment in real water and

biological samples may be a unique diagnostic tool in medicinal, environmental, and industrial applications. The body's metabolic markers for zinc ions make it simple to identify Zn<sup>2+</sup> ions in many investigations (proteins, enzymes, and carbohydrates, and so on).<sup>14</sup> Due to the complexity and triviality of most analytical methods used to detect Zn<sup>2+</sup> ions, researchers have shifted their focus to fluorescence detection technology, essential for environmental and biological system analysis.

Colorimetric and fluorescent chemosensors based on organic emissive molecules promise innovative solutions for sensor applications, since they are simple to use and can quickly provide chemical information.<sup>15–27</sup> A plethora of fluorescent chemosensors<sup>28–37</sup> has been developed to date based on different fluorophores, such as purine-based Schiff base,<sup>38</sup> rhodamine,<sup>39</sup> aminomethylnaphthol,<sup>40</sup> coumarin,<sup>41</sup> and quinoline containing acetyl hydrazone.<sup>42</sup> One frequent obstacle in searching for Zn<sup>2+</sup>-detection ligands is their apparent inability to distinguish Zn<sup>2+</sup> from its chemically identical neighbour, Cd<sup>2+</sup>. Further limiting issues, including multi-step synthesis, employment of a metal–ligand ensemble for recognition, poor chemical stability, and insignificant detection limitations, have been frequently found in a large percentage of scientific publications that assess the effectiveness of prospective Zn<sup>2+</sup> sensing molecules.

Benzothiazole<sup>43–51</sup> and imidazole<sup>52–58</sup> derivatives have been intensively implemented in the development of optical chemosensors due to their easy functionalization and photostability. They are particularly effective in chelating metal ions because of sulfur, oxygen, and nitrogen atoms with lone-pair of

<sup>a</sup>Department of Chemistry, School of Advanced Sciences and Vellore Institute of Technology, Vellore-632014, India. E-mail: sathiya\_kuna@hotmail.com

<sup>b</sup>Department of Chemistry, Faculty of Science, Chulalongkorn University, Phayathai Rd., Pathumwan, Bangkok, 10330, Thailand. E-mail: pra3sat@gmail.com

<sup>c</sup>Department of Chemistry, Saveetha School of Engineering, Saveetha Institute of Medical and Technical Sciences (SIMATS), Chennai-602 105, Tamil Nadu, India

† Electronic supplementary information (ESI) available. See <https://doi.org/10.1039/d2ra04874d>



electrons. We hypothesized that the imidazole conjugated benzothiazole moiety might be used to detect  $\text{Zn}^{2+}$  in an aqueous solution since they are expected to bind metal ions strongly and have excellent photophysical properties.

As part of our research interest in ion recognition,<sup>59–63</sup> in this work, we utilize benzothiazole-linked imidazole as a fluorophore to design and construct a “turn-on”  $\text{Zn}^{2+}$  fluorescence probe. The structure of the synthesized probe forms an excellent conjugated system through benzothiazole and imidazole pyridine and results in a strong photon-induced electron transfer (PET) action, which interferes with the probe's fluorescence emission. This novel  $\text{Zn}^{2+}$  sensor is promising due to its rapid response to  $\text{Zn}^{2+}$ , excellent sensing capability and simplicity of preparation. The sensor, named **BIPP** in this manuscript, was used to demonstrate the applicability by detecting  $\text{Zn}^{2+}$  in water, test strips, and live cells, providing a dependable method for detecting  $\text{Zn}^{2+}$  in environmental and biological systems.

## 2. Experimental section

### 2.1. Materials and methods

Di(pyridin-2-yl) methanone, all the other chemicals and solvents were obtained from commercial suppliers (Sigma Aldrich and TCI chemicals) and used without further purification.  $^1\text{H}$  and  $^{13}\text{C}$  NMR analyses were performed in Bruker 400 MHz and 100 MHz instruments. NMR spectra were stated in parts per million (ppm,  $\delta$ ). UV-Vis absorption spectra were monitored with the help of Hitachi-2910 spectrophotometers, and emission spectra were monitored with Hitachi F-7000 spectrophotometers. High-Resolution Mass Spectrometer (HRMS) data were collected using a Joel GC Mate II GC-Mass Spectrometer instrument.

### 2.2. Synthesis and characterization

**2.2.1 Preparation of 2-(benzo[*d*]thiazol-2-yl) phenol (BTP).** The reactants 2-amino thiophenol (1.1 ml, 1 mmol) and salicylaldehyde (1 ml, 1 mmol) were dissolved in 15 ml of EtOH. This reaction mixture was kept under reflux for 5 hours. The progress of the reaction was examined by TLC. A white colour solid had been obtained (1.6 g, 84% yield).  $^1\text{H}$  NMR (400 MHz,  $\text{DMSO}-d_6$ ): 6.991–7.7.010 (t, 1H,  $J = 7.6$  Hz), 7.097–7.118 (d, 1H,  $J = 8.4$  Hz), 7.392–7.413 (q, 2H,  $2x\text{ArCH}$ ,  $J = 8.4$  Hz), 7.510–7.512 (t, 1H,  $J = 1.6$  Hz), 8.050–8.070 (d, 1H,  $J = 8$  Hz), 8.109–8.129 (t, 2H,  $J = 8$  Hz), 11.652 (s, 1H, OH).  $^{13}\text{C}$  NMR ( $\text{DMSO}-d_6$ , 100 MHz):  $\delta$  117.48, 118.70, 120.20, 122.43, 122.57, 125.57, 126.92, 129.00, 132.94, 134.61, 151.91, 156.82, 165.92.

**2.2.2 Synthesis of 3-(benzo[*d*]thiazol-2-yl)-2-hydroxybenzaldehyde (BTH).** The Compound **BTP** (2 g, 1 mmol) was dissolved in acetic acid (20 ml), followed by the addition of hexamethylenetetramine (2.19 g, 2 mmol). The reaction mixture was refluxed for 5 hours. The completion of the reaction was inspected by TLC. After that, the reaction mixture was allowed to cool in room temperature, and it was poured into crushed ice with vigorous stirring. The filtered solid product was purified by column chromatography.<sup>64,65</sup> (1.2 g, 53%).  $^1\text{H}$

NMR (400 MHz,  $\text{DMSO}-d_6$ ):  $\delta$  7.218–7.237 (t, 1H,  $J = 7.6$  Hz), 7.505–7.523 (t, 1H,  $J = 7.2$  Hz), 7.588–7.606 (t, 1H,  $J = 7.2$  Hz), 7.919–7.938 (d, 1H,  $J = 7.6$  Hz), 8.125–8.145 (d, 1H,  $J = 8$  Hz), 8.207–8.227 (d, 1H,  $J = 8$  Hz), 8.385–8.404 (d, 1H,  $J = 7.6$  Hz), 10.378 (s, 1H, OH), 13.006 (s, 1H, CHO).  $^{13}\text{C}$  NMR ( $\text{DMSO}-d_6$ , 100 MHz):  $\delta$  119.71, 120.71, 122.79, 122.82, 123.94, 126.39, 127.46, 133.43, 133.94, 135.58, 151.43, 159.50, 165.79, 192.27.

**2.2.3 2-(benzo[*d*]thiazol-2-yl)-6-(1-(pyridin-2-yl) imidazo[1,5-*a*] pyridin-3-yl) phenol (BIPP).** In a round bottom flask a mixture of **BTH** (1 g, 3.9 mmol), di(pyridin-2-yl) methanone (0.481 mg, 2.6 mmol) ammonium acetate (1.05 g, 13 mmol) was charged in acetic acid. The suspension was allowed to reflux for 6 h and the reaction was tracked by TLC. Once the reaction was completed the reaction mixture was cooled to room temperature, then poured into crushed ice, stirred for 30 minutes and filtered. The yellow solid was obtained, and then washed with diethyl ether. Yield 60%; mp 270–273 °C;  $^1\text{H}$  NMR (400 MHz,  $\text{CDCl}_3$ )  $\delta$  ppm 6.936–6.918 (t, 1H,  $J = 7.2$  Hz), 7.224–7.208 (m, 1H,  $J = 6.4$  Hz), 7.318–7.304 (t, 2H,  $J = 5.6$  Hz), 7.553–7.533 (m, 1H,  $J = 8$  Hz), 7.622–7.601 (m, 1H,  $J = 8.4$  Hz), 7.872–7.869 (q, 1H,  $J = 8$  Hz), 7.976–7.956 (t, 1H,  $J = 8$  Hz), 8.157–8.139 (q, 2H,  $J = 7.2$  Hz), 8.247–8.226 (m, 3H,  $J = 8.4$  Hz), 8.648–8.636 (t, 2H,  $J = 4.8$  Hz), 7.57–7.55 (d, 1H,  $J = 8$  Hz), 13.151 (s, 1H).  $^{13}\text{C}$  NMR (100 MHz,  $\text{CDCl}_3$ )  $\delta$  ppm 114.36, 118.22, 118.63, 120.11, 120.75, 121.39, 122.63, 122.90, 125.23, 126.50, 127.59, 130.48, 130.63, 133.31, 135.31, 151.42, 155.42, 168.23. HRMS (ESI)  $m/z$ : [ $\text{MH}^+$ ] calcd for  $\text{C}_{34}\text{H}_{24}\text{N}_2\text{OS}$  421.1055; Found: 421.1134.

### 2.3. Stock solution preparation

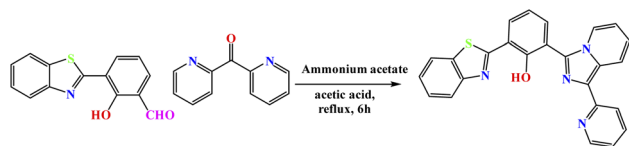
The stock solution of **BIPP** ( $1 \times 10^{-3}$  M) was made by dissolving in the mixture of ACN :  $\text{H}_2\text{O}$  (8 : 2). Aqueous solutions of different nitrate metal cation salts at a concentration of  $1 \times 10^{-3}$  M were made in double-distilled water medium. The fluorescence and absorption were observed in ACN :  $\text{H}_2\text{O}$  (8 : 2) solution. UV-vis absorption and emission were measured using ( $1 \times 10^{-6}$  M) **BIPP** and various metals ( $1 \times 10^{-6}$  M).

## 3. Results and discussion

### 3.1. Synthesis and characterization of the probe BIPP

The benzothiazole unit is particularly advantageous as a component of excited-state intramolecular proton transfer (ESIPT) probe because it is optically stable, environmentally sensitive, and exhibits brilliant fluorescence with a significant Stokes shift. Similarly, the imidazo[1,5-*a*]pyridine nucleus is well-known for its photophysical characteristics in the literature.<sup>66–68</sup> On the basis of these observations, new chemosensor 2-(benzo[*d*]thiazol-2-yl)-6-(1-(pyridin-2-yl) imidazo[1,5-*a*] pyridin-3-yl) phenol (**BIPP**) was developed by incorporating imidazopyridine into the benzothiazole motifs. The imidazopyridine unit is electron-rich and serves as an electron donor, quenching the benzothiazole unit's fluorescence through the photoinduced electron transfer (PET) mechanism. Once **BIPP** coordinates selectively to  $\text{Zn}^{2+}$ , the disruption of the PET process and subsequent generation of the “push–pull” system triggers fluorescence enhancement. Straightforward cyclization





Scheme 1 The synthetic route of sensor BIPP.

of methanones with 3-(benzo[*d*]thiazol-2-yl)-2-hydroxybenzaldehyde in the presence of ammonium acetate was used to accomplish the synthetic process (Scheme 1). The reaction is simple, demanding just one step and no need for catalysts or Lewis acids with high sensitivity. The structural identification of the sensor **BIPP** was verified by  $^1\text{H}$  NMR,  $^{13}\text{C}$  NMR, and HRMS spectra analysis (Fig. S1–S7†).

### 3.2. BIPP as a sensory probe for $\text{Zn}^{2+}$

The UV-vis spectral measurements were carried out in a binary mixture of ACN and  $\text{H}_2\text{O}$  (8 : 2, v/v). **BIPP** receptor absorption spectra display two  $\lambda_{\text{max}}$  bands at 292 nm and 327 nm, caused by  $\pi-\pi^*$  and  $n-\pi^*$  transitions, respectively (Fig. S8†). Adding  $\text{Zn}^{2+}$  to the receptor **BIPP** caused the band at 327 nm to vanish, and a new band at 393 nm emerged. Whereas, the absorption peak at 292 nm remained undisturbed. On the other hand, there were no significant changes in the absorbance spectra of receptor **BIPP** with other examined cations such as  $\text{Ag}^+$ ,  $\text{Na}^+$ ,  $\text{K}^+$ ,  $\text{Li}^+$ ,  $\text{Ba}^{2+}$ ,  $\text{Ca}^{2+}$ ,  $\text{Cd}^{2+}$ ,  $\text{Ce}^{4+}$ ,  $\text{Co}^{2+}$ ,  $\text{Cu}^{2+}$ ,  $\text{Fe}^{2+}$ ,  $\text{Hg}^{2+}$ ,  $\text{Mg}^{2+}$ ,  $\text{Mn}^{2+}$ ,  $\text{Ni}^{2+}$ ,  $\text{Pb}^{2+}$ ,  $\text{Sr}^{2+}$ ,  $\text{Al}^{3+}$ ,  $\text{Cr}^{3+}$ ,  $\text{Fe}^{3+}$  and  $\text{Ru}^{3+}$ , indicating that receptor **BIPP** binds preferentially to  $\text{Zn}^{2+}$  ions while in the ground state  $\text{Zn}^{2+}$  causes electronic perturbation in **BIPP** (Fig. 1a). The progressive addition of  $\text{Zn}^{2+}$  was used to perform UV-vis titration of the receptor **BIPP** in ACN :  $\text{H}_2\text{O}$  (8 : 2, v/v) solution (Fig. 1b). Following the progressive addition of  $\text{Zn}^{2+}$ , the disappearance of the receptors absorption band at 327 nm and the appearance of a new peak at 393 nm were gradual, with the eventual appearance of the isosbestic point at 372 nm. An interaction between  $\text{Zn}^{2+}$  and receptor **BIPP** results in creating isosbestic points, which suggest that new species has been formed.

A fluorescence technique was used to examine the receptor's metal-ion detecting characteristics in similar mixed solvent solutions by adding the nitrate salt of several series of different

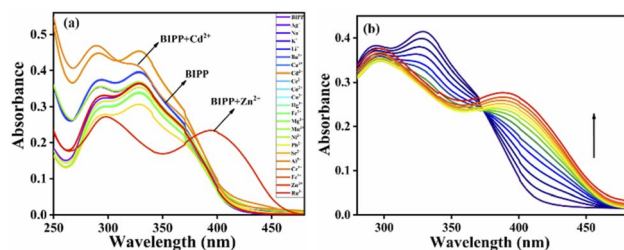


Fig. 1 (a) UV-Vis absorption spectra of sensor BIPP ( $1 \times 10^{-6}$  M) towards 5 equiv. of various anions in ACN/ $\text{H}_2\text{O}$  (8 : 2, v/v) solution; (b) absorption spectra of sensor BIPP ( $1 \times 10^{-6}$  M) in ACN/ $\text{H}_2\text{O}$  (8 : 2, v/v) solution upon the addition of various concentrations of  $\text{Zn}^{2+}$  ions (0–2 equivalents).

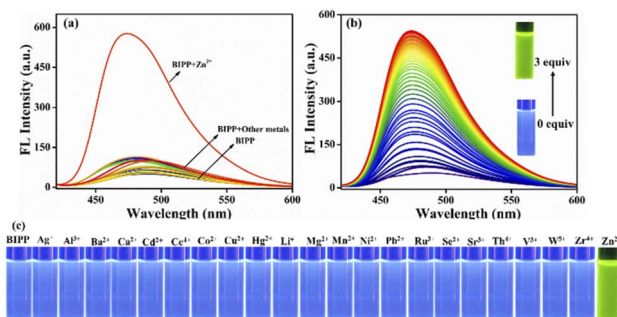


Fig. 2 (a) Fluorescence spectra of BIPP (2.0 M) after the addition of 21 metal ions (5 equiv.) in an ACN/ $\text{H}_2\text{O}$  (8 : 2, v/v) solution. (b) Fluorescent spectra of BIPP (2.0 M) in ACN/ $\text{H}_2\text{O}$  (8 : 2, v/v) solution with different  $\text{Zn}^{2+}$  ions concentrations (0–3 equivalent). (c) Fluorescence bottle images of BIPP in solution with various metal ions ( $1 \times 10^{-3}$  M).

cations including  $\text{Ag}^+$ ,  $\text{Na}^+$ ,  $\text{K}^+$ ,  $\text{Li}^+$ ,  $\text{Ba}^{2+}$ ,  $\text{Ca}^{2+}$ ,  $\text{Cd}^{2+}$ ,  $\text{Ce}^{4+}$ ,  $\text{Co}^{2+}$ ,  $\text{Cu}^{2+}$ ,  $\text{Fe}^{2+}$ ,  $\text{Hg}^{2+}$ ,  $\text{Mg}^{2+}$ ,  $\text{Mn}^{2+}$ ,  $\text{Ni}^{2+}$ ,  $\text{Pb}^{2+}$ ,  $\text{Sr}^{2+}$ ,  $\text{Al}^{3+}$ ,  $\text{Cr}^{3+}$ ,  $\text{Fe}^{3+}$  and  $\text{Ru}^{3+}$  (Fig. 2a). Due to the prevailing photo-induced electron transfer (PET) mechanism at the excited state, the receptor **BIPP** exhibited faint fluorescence after being stimulated at 489 nm. The receptor **BIPP** demonstrated an extremely selective 'Off-On' fluorescence increase at 473 nm in the presence of  $\text{Zn}^{2+}$  among the different metal ions tested (5 equivalents). Additionally, the fluorescence titration of receptor **BIPP** was carried out by adding  $\text{Zn}^{2+}$  ions progressively over time (Fig. 2b). The fluorescence band at 489 nm of the receptor **BIPP** increased with increasing  $\text{Zn}^{2+}$  concentration. Notably,  $\text{Zn}^{2+}$  concentration alters the fluorescence intensity of **BIPP** linearly between 0.1 and 1  $\mu\text{M}$ . An excellent linear correlation between the relative fluorescence intensities ( $I/I_0$  at 473 nm) was found using the derived calibration curve for the concentration range of 0.1 to 1  $\mu\text{M}$  of  $\text{Zn}^{2+}$  ion (Fig. S9†). We found the linear equation is  $y = 7.05697x + 0.62667$ , where  $x$  is the concentration of  $\text{Zn}^{2+}$  and  $y$  is the absorption intensity at 473 nm. For the sensor **BIPP**, the detection limit was determined by taking the slope of the linear fit graph and the standard deviation from the blank **BIPP** fluorescence spectra, as shown in eqn (1) (see ESI†). The LOD was  $2.36 \times 10^{-8}$  M, far below the WHO's recommended limit of 76.5  $\mu\text{M}$ .<sup>69</sup> It was discovered that the achieved detection limit was significantly lower than that reported in current literature (Table S1†). With the addition of  $\text{Zn}^{2+}$ , **BIPP**'s solution has changed color under ultraviolet light from blue to bright green (Fig. 2c). The quantum yield of **BIPP**, on the other hand, increased dramatically when  $\text{Zn}^{2+}$  was added ( $\Phi = 0.68$ ).

### 3.3. Effects of competitive metal ions, pH, and time response

A chemosensor must, among other things, respond specifically to target analytes while avoiding cross-sensitivity. Hence, the competitive experiment was conducted by taking fluorescence spectrum readings of receptor **BIPP** in 1 equivalent with  $\text{Zn}^{2+}$  combined with other interfering cations, as stated above (Fig. 3a). No substantial difference was observed between  $\text{Zn}^{2+}$  solutions with and without other cations in the fluorescence



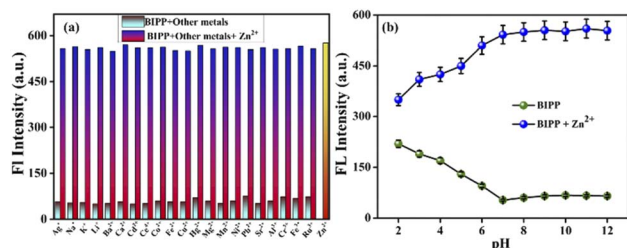


Fig. 3 (a) Competitive assays for the fluorescence responses of BIPP (1  $\mu\text{M}$ ) in the presence of  $\text{Zn}^{2+}$  ions (1  $\mu\text{M}$ ) and other competing metal ions (5  $\mu\text{M}$ ) in ACN/ $\text{H}_2\text{O}$  (8 : 2, v/v) solution. (b) In the absence and presence of  $\text{Zn}^{2+}$ , the influence of pH on the fluorescence intensity of BIPP in ACN/HEPES buffer (8 : 2) (pH 2.0–12.0) solutions.

spectra of receptor **BIPP**. These findings suggest that other potentially competing cations do not affect receptor **BIPP**'s identification of  $\text{Zn}^{2+}$ . Due to its higher sensitivity for  $\text{Zn}^{2+}$ , receptor **BIPP** may be used in real-time sample analysis. The chemosensor **BIPP** and **BIPP**- $\text{Zn}^{2+}$  system was examined for the effects of pH variation. The chemosensor **BIPP**'s fluorescence pattern in the pH range of 2.0 to 12.0 is depicted in (Fig. 3b). In the pH range of 6.0 to 12.0, the fluorescence spectra of the chemosensor **BIPP** showed no noticeable change. When the pH falls below 6, the additional supply of  $\text{H}^+$  protonates the pyridyl and imidazole nitrogen, increasing the fluorescence. Additionally, adjusting the pH from 2.0 to 6.0 alters the chemosensor **BIPP**'s fluorescence response to  $\text{Zn}^{2+}$  ions. At lower pH levels, the protonation of the pyridyl and imidazole nitrogen hinders complexation with  $\text{Zn}^{2+}$  because there are no lone pair of electrons available. This suggests that when the pH decreases from 6 to 2, the fluorescence of **BIPP** +  $\text{Zn}^{2+}$  increases. The interaction of  $\text{Zn}^{2+}$  ions with the receptor **BIPP** occurred quickly during the first 10 seconds, as shown (Fig. S10<sup>†</sup>), and there was no significant change in fluorescence intensity after that, even when the time period was prolonged to 60 seconds. These results show that the chemosensor **BIPP** has quick coordination with  $\text{Zn}^{2+}$ , which is desired.

## 4. Sensing mechanism

Imidazole-nitrogen and pyridyl-nitrogen are thought to interact with  $\text{Zn}^{2+}$  ions to create a **BIPP**- $\text{Zn}$  complex in solution. When the receptor **BIPP** and the  $\text{Zn}^{2+}$  ion interact, the ICT process speeds up, bringing the lowest excited state closer to the highest ground state.<sup>70,71</sup> To evaluate the manner of complexation directly,  $^1\text{H}$  NMR titrations of **BIPP** with different doses of  $\text{Zn}^{2+}$  in  $\text{DMSO}-d_6$  were performed (Fig. 4). In  $^1\text{H}$  NMR, the pure **BIPP** displayed a hydroxyl ( $-\text{OH}$ ) signal at 13.14 ppm, and the protons flanking the pyridyl nitrogen appeared at 8.73 ppm ( $\text{H}_a$ ) and 8.22 ppm ( $\text{H}_b$ ). But with the increasing concentration of zinc ions, the signal of  $\text{H}_a$  and  $\text{H}_b$  showed a up field shifted from 8.73 ppm to 8.69 ppm and 8.22 ppm to 8.12 ppm. The proton ( $\text{H}_c$ ) located para to the phenolic  $-\text{OH}$  felt an upfield shift from 7.33 ppm to 7.22 ppm. The proton marked as  $\text{H}_d$  also shifted to the upfield region from 6.89 to 6.57 ppm. In addition, the  $-\text{OH}$  signal shifted from 13.14 ppm to 12.38.

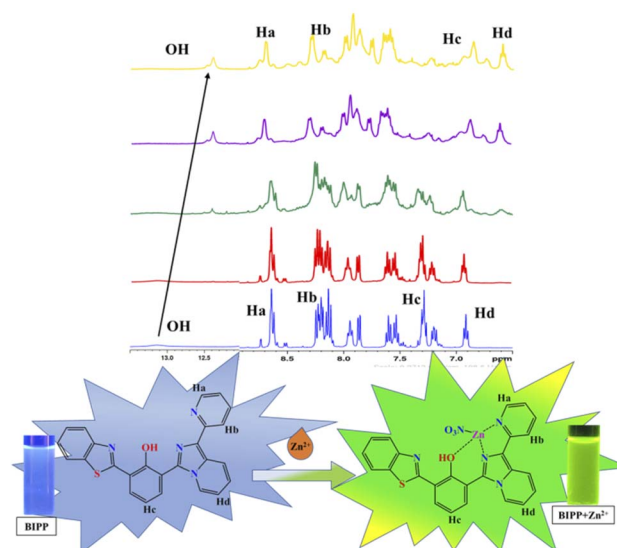


Fig. 4  $^1\text{H}$  NMR spectra of BIPP (400 MHz,  $\text{DMSO}-d_6$ , TMS) and the complex **BIPP**- $\text{Zn}^{2+}$  following the addition of  $\text{Zn}^{2+}$  ions.

This confirms that the complexation happens in the region of imidazole and pyridyl ring. Furthermore, HRMS study confirmed the presence of a **BIPP**- $\text{Zn}^{2+}$  complex (Fig. S11<sup>†</sup>). Positive ion mass analysis indicated that the peak at 546.0209 ( $m/z$ ) was ascribed to  $[\text{BIPP} + \text{Zn}^{2+} + \text{NO}_3]^+$  (calcd, 546.0214). Job plot analysis was used to comprehend the means of binding between the sensor **BIPP** and  $\text{Zn}^{2+}$  (Fig. S12<sup>†</sup>). It was discovered that the binding stoichiometry between **BIPP** and  $\text{Zn}^{2+}$  was 1 : 1. The Benesi-Hildebrand plot of **BIPP** derived from emissive titration data was used to determine the binding constant, which was determined to be  $6.7189 \times 10^5 \text{ M}^{-1}$  between the receptor **BIPP** and the  $\text{Zn}^{2+}$  ion (Fig. S13<sup>†</sup>).<sup>72,73</sup> In the FT-IR spectrum of **BIPP**, the  $\text{OH}$  functional group was attributed at  $3383.48 \text{ cm}^{-1}$ . The  $\text{OH}$  peak did not vanish when **BIPP** interacted with  $\text{Zn}^{2+}$ , indicating that the  $\text{Zn}^{2+}$  ion was combining with only pyridyl nitrogen (Fig. S14<sup>†</sup>).

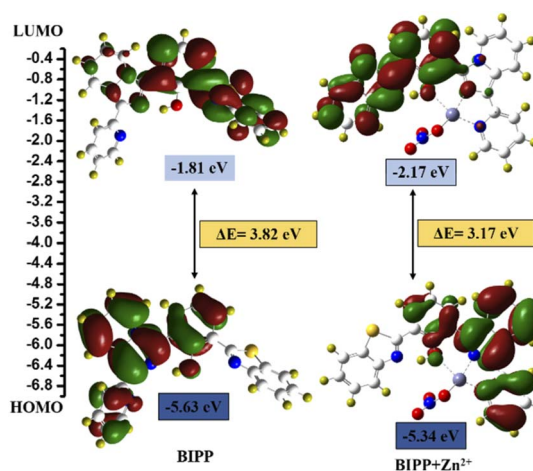


Fig. 5 DFT calculated LUMO and HOMO diagrams of **BIPP** and **BIPP** +  $\text{Zn}^{2+}$ . Application of the proposed method for analysis of environmental water samples.



Table 1 Determination of Zn<sup>2+</sup> ion in regular water samples

Water samples studied	Concentration of standard Zn <sup>2+</sup> ion spiked ( $\mu\text{M}$ )	Concentration of Zn <sup>2+</sup> ion found ( $\mu\text{M}$ ) ( $n = 3$ )	Recovery of Zn <sup>2+</sup> ions added (%)
Tap water	2.0	1.95	97.5
	4.0	3.97	99.25
	6.0	6.03	100.5
Drinking water	2.0	2.02	101
	4.0	4.11	102.75
	6.0	6.21	103.5

In addition, DFT calculations using the Gaussian 09 programme were employed to support the sensing mechanism. The frontier molecular orbital (FMO) analysis of both chemosensors and the target analyte were optimised at the B3LYP/6-31G (d) level of theoretical analysis.<sup>74</sup> Fig. 5 depicts the HOMO–LUMO surfaces of the **BIPP** chemosensor. The HOMO was mainly localized on the imidazo pyridine of the chemosensor units, and the LUMO orbital was dispersed over benzothiazole which accounts for the extended  $\pi$  conjugation. The HOMO orbital of the chemosensor units was mostly centred on the imidazo pyridine, while the LUMO orbital was spread across benzothiazole, which accounts for the extended conjugation. Similarly, in **BIPP** + Zn<sup>2+</sup> complex, the electronic density of HOMO orbital is dispersed on the imidazo pyridine and on benzothiazole in LUMO orbitals. It is important to note that in the LUMO of the **BIPP** + Zn<sup>2+</sup> complex, the electron density is completely orientated towards benzothiazole, making the PET process unfeasible. In addition, the energy gaps ( $\Delta E$ ) between HOMOs and LUMOs of **BIPP** and **BIPP** + Zn<sup>2+</sup> were computed to be 3.82 eV and 3.17 eV, respectively. In the presence of Zn<sup>2+</sup>, the decreased energy gap was responsible for the red-shift spectral transformation in the absorption and emission spectra of **BIPP**.

## 5. Practical sample applications

To further evaluate the use of **BIPP** for determining the Zn<sup>2+</sup> content of actual water samples, recovery tests were conducted using real water samples from tap and drinking water in the Vellore Institute of Technology (VIT), India campus using the previously described approach.<sup>69</sup> For Zn<sup>2+</sup> detection, **BIPP** sensor yielded recoveries of 97.5% to 103.5%, as shown Table 1. The results showed that **BIPP** could be used to detect Zn<sup>2+</sup> in real samples with high accuracy, indicating certain practical value of this probe. These results show that the competing metal ions in the water sample have no effect on the accuracy of the sensor we constructed to monitor Zn<sup>2+</sup> ions.

## 6. Cell imaging studies

Zn<sup>2+</sup> ion detection in live cells using fluorescence microscopy was established by conducting fluorescence imaging studies. *E. coli* cells have been used to emulate living cells in this experiment.<sup>75</sup> For 30 minutes at 37 °C, *E. coli* cells were incubated with **BIPP** in PBS with 1% DMSO as a co-solvent and imaged. After 30 minutes, the cells were infused with 2  $\mu\text{M}$  Zn<sup>2+</sup> and imaged once again.

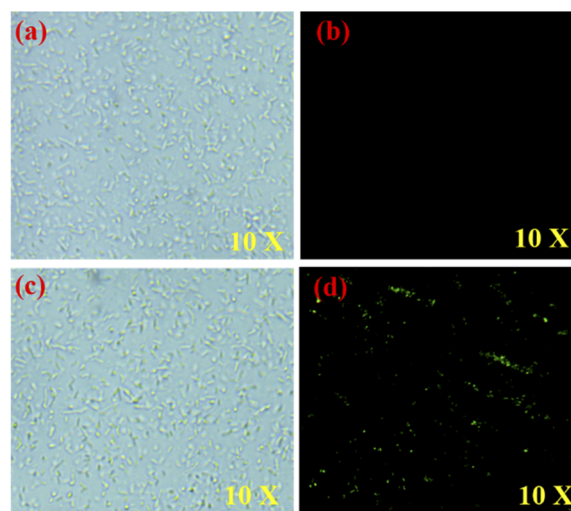


Fig. 6 This picture shows bright-field and fluorescence images of *E. coli* cells that have been exposed to **BIPP** and Zn<sup>2+</sup>. (a and c) *E. coli* cells were incubated separately with **BIPP** and **BIPP** + Zn<sup>2+</sup> (b) *E. coli* cells were treated with **BIPP** (d) *E. coli* cells were treated with **BIPP** and Zn<sup>2+</sup>.

Incubation of *E. coli* cells with **BIPP** did not cause a spike in intracellular fluorescence, as was anticipated (Fig. 6b). On the other hand, when **BIPP**-loaded *E. coli* cells were incubated with Zn<sup>2+</sup>, a bright greenish-yellow fluorescence was seen (Fig. 6d). Thus, it is clear that the fluorescence increase in live cells was caused by the complexation of **BIPP** with Zn<sup>2+</sup>. In cytotoxicity experiments (Fig. S15<sup>†</sup>), **BIPP** was shown to be highly biocompatible and non-toxic to live cells. Thus, the appearance of significant fluorescence inside the intracellular region suggests that the probe **BIPP** is capable of detecting Zn<sup>2+</sup> ions in living cells.

## 7. Conclusion

Finally, we have devised and synthesized a new and simple benzothiazole conjugated imidazopyridine **BIPP** with tunable absorbance and fluorescence to detect Zn<sup>2+</sup> ions. An increase in fluorescence intensity of **BIPP** at 473 nm resulted from the addition of Zn<sup>2+</sup>, which disturbed the PET process and caused the fluorescence color shift from blue to bright green. Besides, probe **BIPP** demonstrated superior Zn<sup>2+</sup> specific selectivity and sensitivity in semi-aqueous conditions when compared to other



competitive metal ions with a lower detection limit ( $2.36 \times 10^{-8}$  M). The **BIPP** +  $\text{Zn}^{2+}$  complexation process was confirmed by electronic spectral titration, Job's plot,  $^1\text{H}$  NMR, and HRMS experiments. The efficacy of **BIPP** in imaging the presence of  $\text{Zn}^{2+}$  in *E. coli* and water samples indicates that it has a broad range of application possibilities. According to the findings in this study, we are certain that **BIPP** could be employed for  $\text{Zn}^{2+}$  detection in a variety of applications.

## Conflicts of interest

There are no conflicts to declare.

## Acknowledgements

Saravanan Enbanathan thanks VIT University for providing financial support through research associateship (VIT/HR/Fac.Appt./2021/6876). The DST-FIST NMR facility at VIT University is duly acknowledged. Finally, the authors thank Dr S. Meenakshi, SSL-VIT, for language editing.

## Notes and references

- N. Kaur and B. Kaur, *Microchem. J.*, 2020, **158**, 105131.
- S. Upadhyay, A. Singh, R. Sinha, S. Omer and K. Negi, *J. Mol. Struct.*, 2019, **1193**, 89–102.
- D. Udhayakumari, *Spectrochim. Acta, Part A*, 2020, **228**, 117817.
- P. Roy, *Coord. Chem. Rev.*, 2021, **427**, 213562.
- E. T. Sawey, M. Chanrion, C. Cai, G. Wu, J. Zhang, L. Zender, A. Zhao, R. W. Busuttill, H. Yee and L. Stein, *Cancer Cell*, 2011, **19**, 347–358.
- L. Li, R. Sun, R. Zheng and Y. Huang, *Mater. Des.*, 2021, **205**, 109759.
- V. Gerke, C. E. Creutz and S. E. Moss, *Nat. Rev. Mol. Cell Biol.*, 2005, **6**, 449–461.
- J. M. Berg and Y. Shi, *Science*, 1996, **271**, 1081–1085.
- Y. Chen, Y. Bai, Z. Han, W. He and Z. Guo, *Chem. Soc. Rev.*, 2015, **44**, 4517–4546.
- H. Huang, H. Lei, F. Yang, X. Fan, Q. Dang and Y. Li, *Biomed. Pharmacother.*, 2018, **106**, 1713–1719.
- O. P. Ajsuvakova, A. A. Tinkov, D. Willkommen, A. A. Skalnaya, A. B. Danilov, A. A. Pilipovich, M. Aschner, A. V. Skalny, B. Michalke and M. G. Skalnaya, *J. Trace Elem. Med. Biol.*, 2020, **59**, 126423.
- M. Z. Khan, *Biomed. Pharmacother.*, 2016, **79**, 263–272.
- U. Doboszewska, K. Młyniec, A. Właż, E. Poleszak, G. Nowak and P. Właż, *Pharmacol. Ther.*, 2019, **193**, 156–177.
- X. Qian and Z. Xu, *Chem. Soc. Rev.*, 2015, **44**, 4487–4493.
- S. Khan, X. Chen, A. Almahri, E. S. Allehyani, F. A. Alhumaydhi, M. M. Ibrahim and S. Ali, *J. Environ. Chem. Eng.*, 2021, **9**, 106381.
- A. Roy, M. Nandi and P. Roy, *TrAC Trends Anal. Chem.*, 2021, **138**, 116204.
- X. Gong, X. Ding, N. Jiang, T. Zhong and G. Wang, *Microchem. J.*, 2020, **152**, 104351.
- P. R. Dongare and A. H. Gore, *ChemistrySelect*, 2021, **6**, 5657–5669.
- A. Kumar, S. K. Hira and S. Dey, *Eur. J. Inorg. Chem.*, 2020, **2020**, 3771–3777.
- C. A. S. Pothulapadu, A. Jayaraj, R. N. Priyanka and G. Sivaraman, *ACS Omega*, 2021, **6**, 24473–24483.
- X. He, F. Ding, X. Sun, Y. Zheng, W. Xu, L. Ye, H. Chen and J. Shen, *Inorg. Chem.*, 2021, **60**, 5563–5572.
- G. Wang, X. Chen, S. Liu, C. Wong and S. Chu, *ACS Nano*, 2016, **10**, 1788–1794.
- J. Su, S. Zhang, C. Wang, M. Li, J. Wang, F. Su and Z. Wang, *ACS Omega*, 2021, **6**, 14819–14823.
- A. C. Di Wu and T. G. Sedgwick, *Chem. Soc. Rev.*, 2017, **46**, 7105–7123.
- P. Kumar, S. Pachisia and R. Gupta, *Inorg. Chem. Front.*, 2021, **8**, 3587–3607.
- M. H. Chua, H. Zhou, Q. Zhu, B. Z. Tang and J. W. Xu, *Mater. Chem. Front.*, 2021, **5**, 659–708.
- A. D. Cabral, T. B. Radu, E. D. de Araujo and P. T. Gunning, *RSC Chem. Biol.*, 2021, **2**, 815–829.
- Y. Li, Z. Yang, Z. Liu, B. Wang and S. Li, *Sens. Actuators, B*, 2011, **160**, 1504–1507.
- P. Mazumdar, S. Maity, D. Das, S. Samanta, M. Shyamal and A. Misra, *Sens. Actuators, B*, 2017, **238**, 1266–1276.
- C. Patra, A. K. Bhanja, C. Sen, D. Ojha, D. Chattopadhyay, A. Mahapatra and C. Sinha, *Sens. Actuators, B*, 2016, **228**, 287–294.
- Q.-F. Li, J.-T. Wang, S. Wu, G.-W. Ge, J. Huang, Z. Wang, P. Yang and J. Lin, *Sens. Actuators, B*, 2018, **259**, 484–491.
- X. Gao, X. Zhuang, C. Tian, H. Liu, W.-F. Lai, Z. Wang, X. Yang, L. Chen and A. L. Rogach, *Sens. Actuators, B*, 2020, **307**, 127626.
- L. Wang, W. Li, W. Zhi, Y. Huang, J. Han, Y. Wang, Y. Ren and L. Ni, *Sens. Actuators, B*, 2018, **260**, 243–254.
- J. Wang, X. Liu and Y. Pang, *J. Mater. Chem. B*, 2014, **2**, 6634–6638.
- A. Gogoi, S. Mukherjee, A. Ramesh and G. Das, *RSC Adv.*, 2015, **5**, 63634–63640.
- K. Mawai, S. Nathani, P. Roy, U. P. Singh and K. Ghosh, *Dalt. Trans.*, 2018, **47**, 6421–6434.
- N. S. Mohamad, N. H. Zakaria, N. Daud, L. L. Tan, G. C. Ta, L. Y. Heng and N. I. Hassan, *Sensors*, 2021, **21**, 311.
- B. Mariammal, A. Shylaja, S. V. Kumar, S. R. Rubina and R. R. Kumar, *J. Heterocycl. Chem.*, 2020, **57**, 3882–3889.
- Z. Wang, S. Cui, S. Qiu and S. Pu, *J. Photochem. Photobiol., A*, 2019, **376**, 185–195.
- S. Park, H. Lee, Y. Yi, M. H. Lim and C. Kim, *Inorg. Chim. Acta*, 2020, **513**, 119936.
- J. Mou, H. Qi, R. Xiang, S. Xu, J. Liu, S. Meng, N. Chen, Y. Xue and D. Pei, *New J. Chem.*, 2021, **45**, 2958–2966.
- X. He, Q. Xie, J. Fan, C. Xu, W. Xu, Y. Li, F. Ding, H. Deng, H. Chen and J. Shen, *Dyes Pigm.*, 2020, **177**, 108255.
- W.-N. Wu, P.-D. Mao, Y. Wang, X.-L. Zhao, Z.-Q. Xu, Z.-H. Xu and Y. Xue, *Spectrochim. Acta, Part A*, 2018, **188**, 324–331.
- Z. Yu, W. Huang, S. Xu and S. Ke, *Microchem. J.*, 2021, **164**, 106009.



## Paper

- 45 S. Li, D. Cao, X. Meng, Z. Hu, Z. Li, C. Yuan, T. Zhou, X. Han and W. Ma, *Spectrochim. Acta, Part A*, 2020, **230**, 118022.
- 46 W. R. Lovett, A. Al Hamd, S. Casa and M. Henary, *Dyes Pigm.*, 2021, **190**, 109268.
- 47 R. Singh, A. Gogoi and G. Das, *RSC Adv.*, 2016, **6**, 112246–112252.
- 48 H.-W. Zheng, Y. Kang, M. Wu, Q.-F. Liang, J.-Q. Zheng, X.-J. Zheng and L.-P. Jin, *Dalt. Trans.*, 2021, **50**, 3916–3922.
- 49 C. Sravani and A. Sivaramakrishna, *ChemistrySelect*, 2017, **2**, 5688–5694.
- 50 B. Suh, D. Choe and C. Kim, *Color. Technol.*, 2021, **137**, 512–519.
- 51 S. Erdemir, S. Malkondu and O. Alici, *Color. Technol.*, 2015, **131**, 32–37.
- 52 C. J. Rha, H. Lee and C. Kim, *Inorg. Chim. Acta*, 2020, **511**, 119788.
- 53 L. Stroea, M. Murariu and V. Melinte, *J. Mol. Liq.*, 2020, **318**, 114316.
- 54 S. A. Khan, Q. Ullah, H. Parveen, S. Mukhtar, K. A. Alzahrani and M. Asad, *J. Photochem. Photobiol., A*, 2021, **406**, 113022.
- 55 J. S. Ganesan, M. Sepperumal, A. Balasubramaniam and S. Ayyanar, *Spectrochim. Acta, Part A*, 2020, **230**, 117993.
- 56 G. Emandi, K. J. Flanagan and M. O. Senge, *Photochem. Photobiol. Sci.*, 2018, **17**, 1450–1461.
- 57 A. O. Eseola, H. Görls, M. Bangesh and W. Plass, *New J. Chem.*, 2018, **42**, 7884–7900.
- 58 R. C. M. Ferreira, S. P. G. Costa, H. Gonçalves, M. Belsley and M. M. M. Raposo, *New J. Chem.*, 2017, **41**, 12866–12878.
- 59 D. Jothi, S. Manickam, S. Sawminathan, S. Munusamy, S. K. A. Kumar and S. K. Iyer, *Dyes Pigm.*, 2022, **197**, 109826.
- 60 D. Jothi, S. Munusamy and S. K. Iyer, *J. Photochem. Photobiol., A*, 2021, **420**, 113491.
- 61 S. Sawminathan, S. Munusamy, S. Manickam, D. Jothi and S. KulathuIyer, *Dyes Pigm.*, 2021, **196**, 109755.
- 62 S. Enbanathan, S. Munusamy, D. Jothi, S. Manoj kumar, A. P. Gopal and S. KulathuIyer, *Dyes Pigm.*, 2022, 110514.
- 63 S. Munusamy, S. Swaminathan, D. Jothi, V. P. Muralidharan and S. K. Iyer, *RSC Adv.*, 2021, **11**, 15656–15662.
- 64 Y. Yang, Y. Feng, Y.-Z. Wang, F.-Z. Qiu, X.-L. Tang, G.-L. Zhang and W.-S. Liu, *Sens. Actuators, B*, 2017, **253**, 1055–1062.
- 65 Y. Wang and S. Yang, *Chem. Phys. Lett.*, 2020, **761**, 138024.
- 66 A. M. Blanco-Rodriguez, H. Kvapilova, J. Sykora, M. Towrie, C. Nervi, G. Volpi, S. Zalis and A. Vlcek Jr, *J. Am. Chem. Soc.*, 2014, **136**, 5963–5973.
- 67 C. Garino, T. Ruiu, L. Salassa, A. Albertino, G. Volpi, C. Nervi, R. Gobetto and K. I. Hardcastle, *Eur. J. Inorg. Chem.*, 2008, 3587–3591.
- 68 G. Volpi, C. Garino, L. Salassa, J. Fiedler, K. I. Hardcastle, R. Gobetto and C. Nervi, *Chem.-Eur. J.*, 2009, **15**, 6415–6427.
- 69 V. Gite, N. Khairnar, A. Basu, A. Kuwar, N. Singh, J. Singh, B. Bondhopadhyay, K. Tayade and S. K. Sahoo, *Dalton Trans.*, 2015, **44**, 2097–2102.
- 70 M. Patil, S. Bothra, S. K. Sahoo, H. A. Rather, R. Vasita, R. Bendre and A. Kuwar, *Sens. Actuators, B*, 2018, **270**, 200–206.
- 71 S. Seenan and S. Kulathu Iyer, *J. Org. Chem.*, 2020, **85**, 1871–1881.
- 72 F. dos Santos Carlos, L. A. da Silva, C. Zanlorenzi and F. S. Nunes, *Inorg. Chim. Acta*, 2020, **508**, 119634.
- 73 Y. Oubelkacem, T. Lamhasni, A. El Bakkali, S. A. Lyazidi, M. Haddad and A. Ben-Ncer, *Spectrochim. Acta, Part A*, 2021, **247**, 119093.
- 74 S. Enbanathan, S. Manickam, S. Munusamy, D. Jothi, S. Manoj Kumar and S. Kulathu Iyer, *New J. Chem.*, 2022, **46**(14), 6570–6576.
- 75 D. Jothi, S. Munusamy, S. Manoj kumar, S. Enbanathan and S. Kulathu Iyer, *RSC Adv.*, 2021, **12**(14), 8570–8577.

